IOPscience iopscience.iop.org

Home Search Collections Journals About Contact us My IOPscience

Gap-Dependent Terahertz Pulses from Mid-Size-Gap Multi-Energy Arsenic-Ion-Implanted GaAs Antennas

This content has been downloaded from IOPscience. Please scroll down to see the full text.

2008 Jpn. J. Appl. Phys. 47 8419

(http://iopscience.iop.org/1347-4065/47/11R/8419)

View the table of contents for this issue, or go to the journal homepage for more

Download details:

IP Address: 140.113.38.11
This content was downloaded on 25/04/2014 at 14:25

Please note that terms and conditions apply.

Japanese Journal of Applied Physics
Vol. 47, No. 11, 2008, pp. 8419–8425

©2008 The Japan Society of Applied Physics

# Gap-Dependent Terahertz Pulses from Mid-Size-Gap Multi-Energy Arsenic-Ion-Implanted GaAs Antennas

Rone-Hwa CHOU and Ci-Ling PAN*

*Department of Photonics and Institute of Electro-Optical Engineering, National Chiao Tung University, 1001 Ta Hsueh Road, Hsinchu 300, Taiwan, R.O.C.*

(Received May 22, 2008; revised July 10, 2008; accepted July 15, 2008; published online November 14, 2008)

We investigated the characteristics of sub-picosecond radiation pulses from mid-size-gap multi-energy arsenic-ion-implanted GaAs photoconductive antennas in terahertz time-domain spectroscopy experiments. At fixed fluence excitation, both the bandwidth and the negative peak of terahertz waveform minimum reveal increasing trends with increases in the antenna's gap. We reproduce both the measured terahertz waveforms and increasing trends numerically, by calculating a model that incorporates the trap-enhanced bias field with wave equation. We deduce from our simulation that the gap-dependent behavior stems from the fact that an antenna with a larger gap has a stronger trap-enhanced bias field near the anode edge and thereby induces a larger space-charge screening effect and bandwidth. [DOI: 10.1143/JJAP.47.8419]

KEYWORDS: photoconductive antenna, terahertz, multi-energy arsenic-ion-implanted GaAs (multi-GaAs:$As^+$), femtosecond, full-wave model, space-charge screening

## 1. Introduction

Biased photoconductive (PC) antenna is a type of terahertz (THz) radiation emission device widely used in various disciplines like THz time-domain spectroscopy (THz-TDS),[1] THz scale ranging,[2,3] and imaging,[4] and as a result, it has been the central subject of an enormous number of theoretical and experimental investigations. Numerous studies on biased PC antennas have indicated that the THz emission characteristics are associated with the antenna's geometry, PC material, or optical excitation condition. Thus, a thorough understanding of the effect of these three factors on THz radiation emission is essential for scientists to control the THz radiation properties for optimum condition.

For the sake of generating giant THz radiation fields of up to a hundred kilovolts per centimeter, the gap size ($G$) of a biased PC antenna should be larger than 1 cm at least.[5] In a practical experimental configuration for such a large-aperture antenna, one requires a high bias voltage supply and femtosecond optical regenerative amplifier to obtain high THz power, while also employing a parametric generator and cooling system to tune excitation wavelength and remove excessive heat from antennas, respectively. In contrast, the experimental setup for a small-gap antenna ($G < 0.05$ mm) is compact, but the THz radiation power from small-gap biased PC antennas is considerably lower than that from large-aperture ones.[6–8] Therefore, a compromise between large-aperture and small-gap biased PC antennas is to choose mid-size-gap PC antennas ($0.05\,\text{mm} < G < 2\,\text{mm}$) as THz emission sources to avoid employing a bulky system for a large-aperture antenna, while benefiting from its higher THz radiation compared with that of a small-gap antenna. Besides, a mid-size-gap PC antenna offers the significant advantages of being easily fabricated, optically aligned, as well as easily tunable for THz radiation power in contrast to nonlinear crystal-based THz emitters, and thus, it has sparked considerable interest.

One typical material fabricated on biased PC antennas is known as semi-insulating GaAs (SI-GaAs), which has the carrier lifetime $\tau_c$ of several picoseconds as a whole, and possesses a markedly reduced parasitic capacitance suitable for a fast device. Through a compensation of shallow acceptors by the intrinsic type of deep donor defect, EL2, the resistivity of the SI-GaAs antenna is able to reach as high as the order of $10^{17}\,\Omega\cdot$cm.[9] A particularly appealing phenomenon is provided when a DC external bias is applied to the electrodes of a SI-GaAs antenna: an enhanced bias field will form near the edge of the anode leading to an enhanced THz radiation when femtosecond laser pump pulses are incident upon the edge of the anode.[10,11] Another type of PC material is the low-temperature-grown GaAs (LT-GaAs). Compared with the SI-GaAs antenna, the LT-GaAs antenna has a larger bandwidth of THz radiation owing to its shorter carrier lifetime (<1 ps), but its disadvantage lies in the lack of reproducible property. To resolve this problem, an alternative material named arsenic-ion-implanted GaAs (GaAs:$As^+$) has been proposed because it can be duplicated by precisely controlling the ion-implanted dose, and it also has good carrier mobility.[12,13]

Under modest pump pulse excitation, a small-gap or mid-size-gap antenna usually exhibits a bipolar THz waveform[14] where the first positive peak originates from the increase in the photoexcited carrier concentration whereas the negative peak is attributed to the decay of the photoexcited carrier concentration, or the screen of bias field. In theoretical analysis, a full-wave model based on Maxwell's equations is one approach to simulate THz radiation pulses.[15] Calculations in ref. 15 inherently produce a bipolar THz waveform, which results from fast carrier recombination rather than space-charge field screening effect, owing to the exclusion of Poisson's equation in their approach. Another approach is known as the drift-Poisson model where THz radiation pulses are deduced from the time derivative of surface transient photocurrent. Although the drift-Poisson model can describe the space-charge screening effect, it does not include any effects induced by pulse propagation. For instance, Rodriguez and Taylor used this model to study the space-charge screening effect in their numerical work;[16] they analyzed the effects of antenna gap sizes on THz waveforms under various pump fluences. In their analysis, they only considered a uniform bias field profile but ignored

*E-mail address: clpan@faculty.nctu.edu.tw

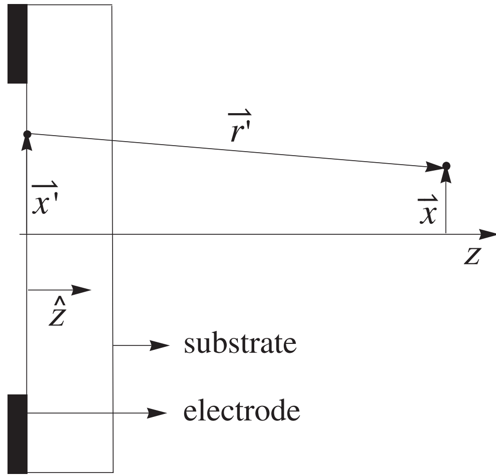


Fig. 1. Geometry for calculating the far-THz field $E_r(t)$. $\boldsymbol{x}'$ is the point on the antenna's surface, $\boldsymbol{x}$ is the observation point, $\boldsymbol{r}'$ is the relative vector of $x'$ with respect to $x$, $r'$ is the distance from $x'$ to $x$, $\hat{z}$ is the normal to the surface, and $ds$ is the differential area on the surface.

any pulse propagation or carrier trapping effect that usually occurs in semi-insulating materials.[17)]

In fact, to our knowledge, there has been little work describing the effect of the antenna's gap size on THz radiation. Hence, the goal of this paper is to elucidate how $G$ affects the characteristics of bipolar THz waveforms under specific situations. In our numerical analysis reported here, we consider the trap-enhanced bias field within antennas, and incorporate the drift-Poisson equation into an electromagnetic wave model[18,19)] to explain quantitatively our experimental data.

## 2. Theoretical Methodology

Figure 1 schematically draws our THz antennas with different bias voltage $V_b$ and $G$. We start from considering how the bias field $E_b$ of multi-GaAs:As$^+$ antennas changes along both the gap direction $x$ and the depth direction $z$ (or the propagation direction of pump pulse) before laser pulse excitation. Provided that a bias voltage $V_b$ is applied to a multi-GaAs:As$^+$-based antenna in the absence of optical pump pulse, the distribution of $E_b$ along $x$ will be nonuniform instead of being simply an average value $V_b/G$. The formation of a nonuniform $E_b$ is due to defects existing within the antenna, thus altering its electrostatic properties including $E_b$ and space-charge concentration. The bias $V$ and $E_b$ have traditionally been determined by utilizing the Poisson equation:

$$-\nabla^2 V = \nabla \cdot E_b = \frac{q}{\varepsilon}[p(x,z) - n(x,z) + N_t(x,z) - N_a^-(x,z)], \tag{1}$$

where $q$ and $\varepsilon$ stand for electron charge and electric permittivity, $p$ and $n$ are the hole and electron concentrations, while the trap and acceptor concentrations are denoted by $N_t$ and $N_a^-$. All the concentrations on the right side of eq. (1) obey Fermi statistics as follows:

$$p(x,z) = N_v\{1 + \exp[(U_f - U_v + qV(x,z))/kT]\}^{-1}, \tag{2}$$

$$n(x,z) = N_c\{1 + \exp[(U_c - U_f + qV(x,z))/kT]\}^{-1}, \tag{3}$$

$$N_t(x,z) = N_{t0}\{1 + \exp[(U_f - U_t + qV(x,z))/kT]\}^{-1}, \tag{4}$$

$$N_a^-(x,z) = N_a\{1 + \exp[(U_a - U_f + qV(x,z))/kT]\}^{-1}, \tag{5}$$

where $N_c$ and $N_v$ are the conduction and valence band effective densities of states, $N_{t0}$ and $N_a$ are the trap and acceptor concentrations, the level of the Fermi energy $U_f$ is determined by letting eq. (1) $= 0$, $U_c$ and $U_v$ are the energy levels of conduction and valence band, and $U_d$ and $U_a$ are the deep donor and shallow acceptor levels. In the literature, depending on the doped concentration or ion-implantation conditions, the $U_d$ values are reported to be about $U_c - 0.670\,\text{eV}$ for SI-GaAs[20)] and $U_c - 0.3\,\text{eV}$ for multi-GaAs:As$^+$.[21)] For our multi-GaAs:As$^+$ antenna, the PC material consists of the multi-GaAs:As$^+$ and SI-GaAs parts. The latter has a thickness of 300 µm, which is very much larger than the former layer (~100 nm). To match the experimental result, $U_d$ and $U_a$ are assumed to be located at $U_c - 0.690\,\text{eV}$ and $U_v + 0.0261\,\text{eV}$. These two values are close to that for the SI-GaAs case because the SI-GaAs part contributes the most to the THz radiation. For a given bias $V_b$, the potential at the anode depends on the maximum field $E_{max}$ at the metal-semiconductor junction owing to image-force lowering, and is given as

$$V(x=0) = V_b + \sqrt{qE_{max}/4\pi\varepsilon}. \tag{6}$$

The solutions of $V_b$ and $E_b$ are obtained by calculating eqs. (1) to (6) iteratively.

When laser pump pulses propagate through the antenna with time $t$, certain amounts of $n$ and $p$ are excited and subjected to electric fields. Both $n$ and $p$ obey the current-continuity equations:

$$\frac{\partial n}{\partial t} = \alpha \bar{I}_{opt}(x,z,t) - \frac{n(x,z,t)}{\tau_c} + \frac{1}{q}\nabla \cdot J_n, \tag{7}$$

$$\frac{\partial p}{\partial t} = \alpha \bar{I}_{opt}(x,z,t) - \frac{p(x,z,t)}{\tau_c} - \frac{1}{q}\nabla \cdot J_p, \tag{8}$$

where $\alpha$ and $\bar{I}_{opt}$ stand for the absorption coefficient and the averaged photogeneration rate, and $J_n$ and $J_p$ are the current densities for electron and hole, respectively. The averaged photogeneration rate $\bar{I}_{opt}$ is defined as

$$\bar{I}_{opt}(x,z,t) \equiv \frac{\int I_{opt}(x,y,z,t)\,dy}{\sqrt{\pi}w_y} = \frac{F(1-R)}{h\nu\sqrt{\pi}w_t}\exp\left[-\left(\frac{x-x_m}{w_x}\right)^2 - \alpha z - \left(\frac{t-z/v}{w_t}\right)^2\right], \tag{9}$$

where $I_{opt}$ is the pump Gaussian beam, and $w_y$ is the beam width in the $y$-direction. The pump Gaussian beam $I_{opt}$ can be expressed in terms of a $w_t$-wide pulse with a $w_x$-wide spatial profile:

$$I_{opt} = \frac{F(1-R)}{h\nu\sqrt{\pi}w_t}\exp\left[-\left(\frac{x-x_m}{w_x}\right)^2 - \left(\frac{y}{w_y}\right)^2 - \alpha z - \left(\frac{t-z/v}{w_t}\right)^2\right]. \tag{10}$$

Here, $F$, $h\nu$, $x_m$, $v$, and $R$ refer to pump fluence, photon energy, position of maximum photogeneration rate, phase velocity of pump pulse, and reflection coefficient, respectively.

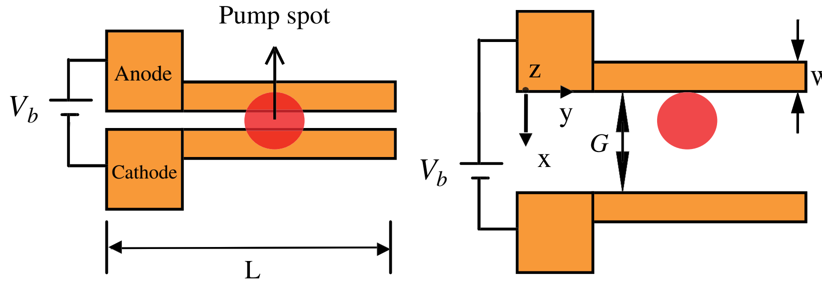


Fig. 2. (Color online) Schematic representation of DC-biased PC antennas excited by femtosecond laser pulses. The transmission line length $L$ and width $W$ are 10 and 0.1 mm, respectively. The illuminated regions are indicated by a red circular spot. The left and right diagrams illustrate a uniform illumination for gap size $G = 0.02$ or 0.1 mm, and an asymmetric illumination for $G = 0.2$ or 0.5 mm, respectively.

In addition to $J_n$ and $J_p$, the separation between n and p also causes a net-charge concentration $\Delta$ ($\equiv$ p − n), which is the main factor that produces the space-charge field $E_s$. The relationship between $E_s$ and $\Delta$ is described using the Poisson equation:

$$\nabla \cdot E_s = \frac{q\Delta}{\varepsilon}. \tag{11}$$

The summation of $J_n$ and $J_p$ in eqs. (7) and (8) is composed of a total current density $J$ that is related to electron and hole mobilities, $\mu_n$ and $\mu_p$, space-charge field $E_s$, and THz field $E$ by the form:

$$J = J_n + J_p = q(\mu_n n + \mu_p p)[E_s(x, z, t) + E(x, z, t)]. \tag{12}$$

In the near-field regime, the creation of $J$ induces a THz field $E$ that satisfies with the wave equation:[22)]

$$\nabla^2 E - \mu\varepsilon \frac{\partial^2 E}{\partial t^2} = \mu \frac{\partial J}{\partial t}, \tag{13}$$

where $\mu$ is the magnetic permittivity. In the far-field regime, the THz radiation field $E_r(t)$ can be obtained by evaluating the broadband Huygen–Fresnel diffraction integral[23)] of near-field $E$ as follows:

$$E_r(t) = \int \frac{\cos(\hat{z}, \boldsymbol{r}')}{2\pi r' c_0} \frac{d}{dt}\left[E\left(\boldsymbol{x}', t - \frac{r'}{c_0}\right)\right] ds. \tag{14}$$

In Fig. 1, we schematically illustrate the quantities used to calculate $E_r(t)$. These quantities include the point $\boldsymbol{x}'$ on the antenna's surface, the observation point $\boldsymbol{x}$, the relative vector $\boldsymbol{r}'$ of $x'$ with respect to $x$, the distance $r'$ from $x'$ to $x$, the normal $\hat{z}$ to the surface, the differential area $ds$ on the surface, and the radiation propagation speed $c_0$ in vacuum. The $\cos(\hat{z}, \boldsymbol{r}')$ term in eq. (14) is known as the obliquity factor. We assume that the observation point locates at the $z$ axis ($\boldsymbol{x} = 0$), and the distance from the antenna's surface to the observation point is assumed to be 60 cm.

While solving eq. (13), a reflection boundary condition was applied to the pump pulse incident surface, and an absorption boundary condition was assumed on the outer surface. In addition, experimental values including $F$, pulse duration $w_t$, carrier lifetime $\tau_c$, and spot size $w_x$ are substituted into eqs. (1)–(14) for each $G$. According to our previous experimental result,[12)] the effective $\mu_n$ is estimated to be 1500 cm$^2$ V$^{-1}$ s$^{-1}$. To match the experimental data, the $\mu_n$ and $\mu_p$ were taken to be 1000 and 30 cm$^2$ V$^{-1}$ s$^{-1}$, the $\alpha$, $v$, $n_L$, and $R$ were $8 \times 10^5$ m$^{-1}$, $8.3 \times 10^7$ m/s, 3.6, and 0.3, respectively.

The positive peak $E_r^{max}$ can be obtained by evaluating the maximum of eq. (14). The relationship between $E_r^{max}$ and $F$ can be approximately described using the scaling rule:[14)]

$$E_r^{max} \approx \frac{F/F_s}{1 + F/F_s}, \tag{15}$$

where the saturation fluence $F_s$ is represented as

$$F_s = \frac{(1 + n_L)h\nu}{q(1 - R)\mu_n \eta_0}. \tag{16}$$

Substituting the effective $\mu_n$ value and $n_L = 3.6$ into eq. (16), we find that $F_s = 25\,\mu$J/cm$^2$.

In calculating eqs. (1)–(14), we consider the two-dimensional ($x$ and $z$) structure without the component in the $y$-direction (the lateral gap direction). This omission is because of the lack of the component of bias field in the $y$-direction. Thus, if the carrier concentration n (or p) and photogeneration rate $I_{opt}$ are both the functions of the $y$-variable in eq. (7), the integration of $I_{opt}(x, y, z, t)$ with respect to $y$ will be equal to an averaged rate $\bar{I}_{opt}(x, z, t)$. In the first term of the left-hand side and the second term of the right-hand side of eq. (7), the integration of $n(x, y, z, t)$ with respect to $y$ will obtain an average carrier concentration $n(x, z, t)$. In addition, the integration of the third term of the right-hand side of eq. (7) with respect to $y$, that is, $\nabla \cdot \int n(x, y, z, t)E_b(x, z, t)\,dy$ will become $\nabla \cdot n(x, z, t)E_b(x, z, t)$ since $E_b$ is dependent on $y$.

## 3. Experimental Methods

We performed the experiments by employing THz time-domain spectroscopy. As illustrated in Fig. 2, the THz radiation emitter consists of two coplanar strip lines with Au metallic coating layers of 300 nm, and was fabricated on multi-energy arsenic-ion-implanted GaAs (multi-GaAs:As$^+$) antenna. When a pump pulse of 800 nm wavelength propagates through the Au coating layer of 300 nm thickness, it will attenuate completely owing to the very shallow skin depth ($\sim$5 nm) of Au and will not be able to excite any carrier beneath the metallic part. In other words, the PC material below the transmission lines will have no contribution to the generation of THz radiation in our case. The transmission line length $L$ and width $W$ are 10 and 0.1 mm, respectively. We chose four samples with different $G$ of 0.02, 0.1, 0.2, and 0.5 mm. Each sample is implanted with an energy of 50, 100 and 200 keV at dosage arsenic ions of $10^{16}$ ions/cm$^2$ and furnace-annealed at 600 °C with 60 min processing. By a transient photo reflectance measurement, the carrier lifetime $\tau_c$ of our multi-GaAs:As$^+$ samples was estimated to be as short as 0.7 ps. The ion implantation depth was estimated to be about 100 nm by secondary ion mass spectroscopy (SIMS) measurement.

To control an average bias field strength $E_b$ ($\sim$ 3.5 kV/cm) to prevent the risk of antenna damage, the $V_b$'s ($= E_b \times G$) applied to the anode were 7, 35, 70, and 175 V

for $G = 0.02$, 0.1, 0.2, and 0.5 mm, respectively. The experimental setup for the generation and measurement of THz radiation was similar to that for the common free space electro-optical (EO) detection[24] from the emitter of biased PC antennas.[25] In detail, the pump or probe pulses of 800 nm wavelength and 130 fs pulse width were also provided by the mode-locked Ti:sapphire laser operating at the repetition rate of 85 MHz and pump power of 500 mW. The pump pulse has a spot size $w_x$ of 0.1 mm diameter and was normally incident upon the antenna's surface. The laser excitation positions are depicted in Fig. 2. In the case of $G = 0.02$ and 0.1 mm, $x_m = G/2$, that is, the spot positions were central with respect to the gap so that both illuminations were nearly uniform. In the case of $G = 0.2$ and 0.5 mm, $x_m = G/4$, the spot positions were off gap center and near the anode, so that both cases belong to edge illuminations. From the values of pump power, spot size, and repetition rate, the pump fluence $F$ was estimated to be 70 μJ/cm$^2$, corresponding to a generated carrier concentration of $2.0 \times 10^{18}$ cm$^{-3}$. Thus, the pump fluence ($F = 70$ μJ/cm$^2$) used in the experiment is considerably larger that the saturation fluence ($F_s = 25$ μJ/cm$^2$) estimated from eq. (16). The generated THz radiation beam was thus collimated and focused onto the EO sensor of ZnTe with a thickness of 1.5 mm by a pair of off-axis paraboloidal mirrors with 12 cm focal length. The distance between the emitter and EO sensor is approximately 50 cm. Since the THz radiation was collected by parabolic mirrors in this experiment, the temporal resolution would be limited by group velocity mismatch between the optical probe beam and THz radiation. The other coherent polarized probe beam was collimated onto the EO crystal and the polarization was modified because of the modified refractive index from the THz field. The probe beam was then transmitted through the analyzer and sampled the THz field from the time delay between the pump and probe beam.

## 4. Results and Discussion

### 4.1 *Trap-enhanced bias field*

Before presenting the experimental data, we analyze our system on the basis of numerical results. Figure 3 shows on a logarithmic scale the simulated bias field $E_b(x)$ as a function of position $x$ for four different $G$ in the absence of pump pulse excitation. Each $E_b(x)$ in Fig. 3 is near the edge of the anode ($0 \leq x \leq 10$ μm) and at depth $z = 0.1$ μm. As seen in this figure, the $E_b(x)$ established near the anode is highly nonuniform. For different values of $G$, one can find much stronger $E_b(x)$ with the larger $G$. Besides, one common feature in all the cases is that the $E_b(x)$ will grow very rapidly if $x$ approaches the anode ($x \sim 0$). For instance, $E_b(x)$ reaches a field strength of as high as $10^3$ kV/cm at $x < 0.5$ μm in the case of $G = 0.5$ mm. This gap-dependent strong bias field is a consequence of the PC antennas with larger $G$ being applied with larger bias voltage.

Because the absorption coefficient of the PC material is about $10^6$ m$^{-1}$, the main absorption range of pump pulses is from $z = 0$ to 2 μm, and is relatively much smaller than the antenna's gap size. Thus, for a given $x$, $E_b$ is uniform along the $z$-direction within this absorption range. This is somewhat similar to the distribution of the magnetic field generated from a magnetic bar. Provided that the length of a magnetic bar is 20 cm, then the magnetic field will be uniform near the bar.

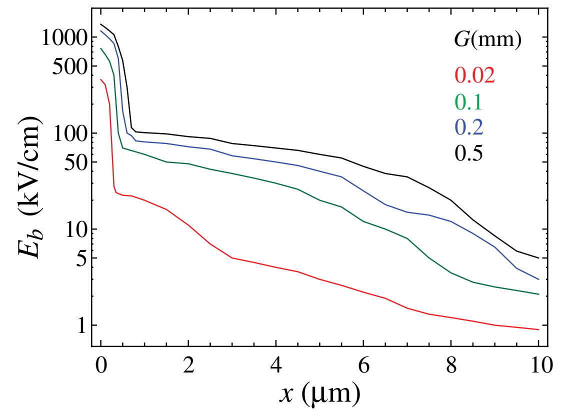


Fig. 3. (Color online) Simulated bias field $E_b(x)$ as a function of position $x$ at depth $z = 0.1$ μm for multi-GaAs:As$^+$ antennas with gap sizes of 0.02 (blue), 0.1 (green), 0.2 (red), and 0.5 mm (black).

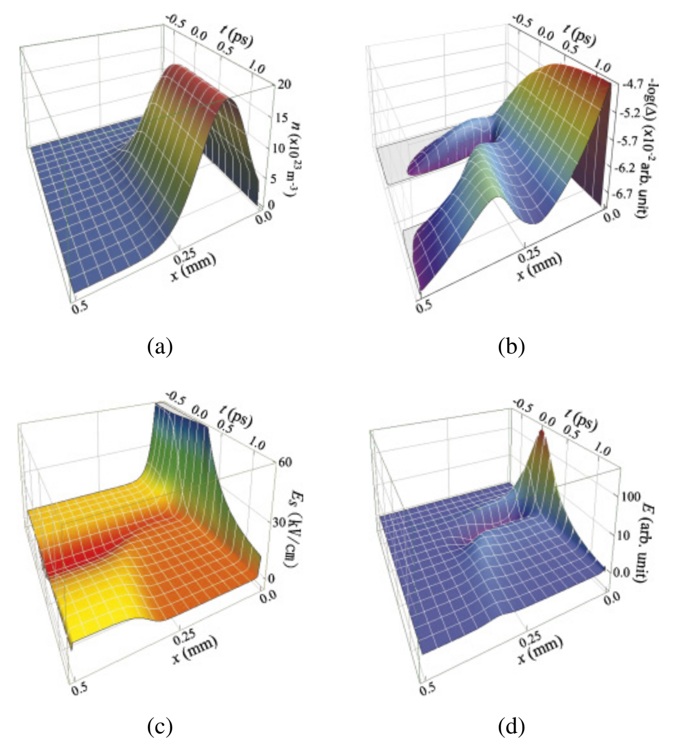


Fig. 4. (Color online) Simulation results. (a) Electron concentration $n(x,t)$, (b) negative logarithmic function of the net-charge concentration, $-\log[\Delta(x,t)]$, (c) space-charge field $E_s(x,t)$, and (d) near-field THz radiation $E(x,t)$ as a function of the time delay $t$ and gap position $x$ at pump depth $z = 0.1$ μm for multi-GaAs:As$^+$ antenna with gap size of 0.5 mm. The values of the large and small peaks in (b) correspond to net-charge concentrations of $1.5 \times 10^{15}$ and $4.0 \times 10^{13}$ cm$^{-3}$, respectively.

### 4.2 *Evolutions of parameters in antennas*

Next, we study the variations of some physical parameters with time at a specific pump depth $z$ and pump fluence $F$. As an example, Fig. 4 shows the calculated $n(x,t)$, $\Delta(x,t)$, $E_s(x,t)$, and $E(x,t)$ for the case of $G = 0.5$ mm. As can be seen from Fig. 4(a), at $x = 0.12$ mm, the photoexcited electron concentration $n$ exhibits a maximum peak, which is the signature of an edge illumination. After excitation, both the photoexcited electron and hole are subjected to $E_s$

and thus move in opposite directions since both possess opposite charges. Of importance, the carrier separation leads to two positive peaks in $\Delta$ as depicted in Fig. 4(b) where one peak locates at around the gap center and the other peak is near the anode. Obviously, the magnitude of the peak near the anode is much larger than that of the central peak. The large peak has a magnitude of $10^2$ of the small peak. This extremely large peak arises from the combination of three mechanisms: the first is that electron mobility is much larger than hole mobility, the second is that the enhanced bias field near the anode speeds up the movement of electron near the anode, and the third is that large amounts of electrons are absorbed by the anode.

The space-charge bias-field screening phenomenon associated with the two $\Delta$ peaks is demonstrated in Fig. 4(c). We can see from this figure that the nonuniform bias field $E_s$ diminishes from its initial value $E_b$ to a lower value with $t$. This behavior originates from the mechanism that the small $\Delta$ peak at the gap center produces an opposite field canceling out the original field between the gap center and anode, while the large $\Delta$ peak near the anode creates a strong opposite field that screens the original enhanced bias field near the anode. The near-field THz radiation $E$ was obtained from the solution of eq. (12), with the result presented in Fig. 4(d). It is clear that inasmuch as the electron and bias field have extreme values near the anode, the maximum $E$ also occurs in the vicinity of the anode.

Let us turn to what is the key to the understanding of the gap-dependent THz waveform, the variations of $\Delta$ and $E_s$ with $t$ at specific $z$ and $x$ near the anode. Substituting four different values of $G$ into the calculations, we obtain the $t$ dependence of $\Delta$ and $E_s$ at $x = 0.01$ mm and $z = 0.1$ µm as shown in Fig. 5. For each $G$, one sees that the quantity $\Delta$ increases from 0 to $1.6 \times 10^{15}$ cm$^{-3}$ with $t$. For different $G$, the larger the $G$, the larger the $\Delta$. The increase in $\Delta$ with $t$ is related to the fast decrease in $E_s$, which is also plotted in Fig. 5. The result of Fig. 5 indicates that the decreasing amount of $E_s$ is proportional to $G$ within a certain time duration. In other words, it implies that an antenna with larger $G$ also has a larger space-charge screening effect that

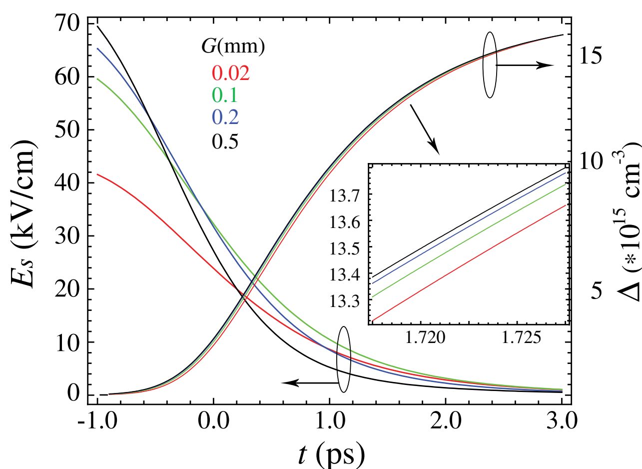


Fig. 5. (Color online) Simulated temporal evolutions of (a) $\Delta(t)$ and (b) $E_b(t)$ at $x = 0.01$ mm and $z = 0.1$ µm for gap sizes of 0.02 (blue), 0.1 (green), 0.2 (red), and 0.5 mm (black). Inset shows a magnified view at $t \sim 1.72$ ps.

significantly affects the THz radiation waveform $E_r$, as we will show in the following.

### 4.3 *THz radiation waveforms and spectra*

On the basis of eq. (13), we calculated the temporal THz fields $E_r$ and corresponding Fourier-transformed amplitude $\tilde{E}_r$ spectra using four different values of $G$, and the results of these calculations are given in Figs. 6(a) and 6(b), respectively. For comparison, we present the measured $E_r$ and their corresponding $\tilde{E}_r$ in Figs. 6(c) and 6(d). Here, we first analyze the measured data. In Fig. 6(c), each measured waveform contains a dominant positive peak and a negative peak followed by a slowly varying tail. The dimensionless parameter $E_r$ was obtained by normalizing individual waveform to its maximum amplitude, so that the maximum amplitude of $E_r$ is equal to one. In the time domain, the analysis for these waveforms can be characterized in terms of four quantities: the positive peak width (full width of the positive peak at half maximum) $\delta_p$, negative peak width (full width of the negative peak at half minimum) $\delta_n$, negative tail with duration of $\Gamma$, and negative value $-E_r^{\min}$ of the negative peak. In the frequency domain, we concentrate on the frequency bandwidth $\Delta f$ of the spectrum (full width of the spectrum at half maximum).

By examining the measured positive and negative peaks in Fig. 6(c), it is worth noting that the inequality $\delta_p > \delta_n$ is always satisfied at different values of $G$. In detail, we observe that the measured $\delta_p$ values are fixed to about 0.33 ps, which is less than that reported from Katzenellenbogen and Grischkowsky ($\delta_p \sim 0.38$ ps).[26] Furthermore, for different $G$, the measured values of $\delta_n$ are also different, and range irregularly between 0.30 to 0.27 ps without any explicit dependence. For each $G$, one can see from Fig. 6(c) that a relatively long negative tail with duration $\Gamma \sim 3.7$ ps follows the negative peak, and is more obvious than those found in other similar experiments.[14,26]

Let us now return to analyze the simulated data. From the simulated waveforms shown in Fig. 6(a), we found $\delta_p > \delta_n$ that is consistent with the measured result. Besides, the simulated data can reproduce the measured long negative tails. Quantitatively, the simulated $\delta_p$, $\delta_n$, and $\Gamma$ are about 0.25, 0.18, and 0.8 ps, respectively. While further simulating the model by varying $F$, we found that the numerical solution gives the result of $\delta_p > \delta_n$ at sufficiently large $F$ ($>10$ µJ/cm$^2$), but a reverse result, $\delta_p < \delta_n$, will be obtained at small $F$ ($<10$ µJ/cm$^2$). In addition, the simulated positive peak $E_r^{\max}$ will vary in a nonlinear way that obeys the scaling rule at various $F$ as the case of small-gap or large-aperture antennas. On the other hand, as $F$ increases, the negative value $-E_r^{\min}$ of the simulated negative peak exhibits an increasing trend since a larger $F$ will excite a larger carrier concentration and thus acquire a larger space-charge field screening effect.

### 4.4 *Dependence of the negative peak on gap size*

Also found in Fig. 6 is the phenomenon that the value of $-E_r^{\min}$ varies with $G$, as well as the bandwidth $\Delta f$. The dependences of both the simulated $r$ and $\Delta f$ on $G$ can be obtained from Figs. 6(a) and 6(b). In Fig. 7, we compare these simulated dependences with the measured ones obtained from Figs. 6(c) and 6(d). As can be seen, as $G$

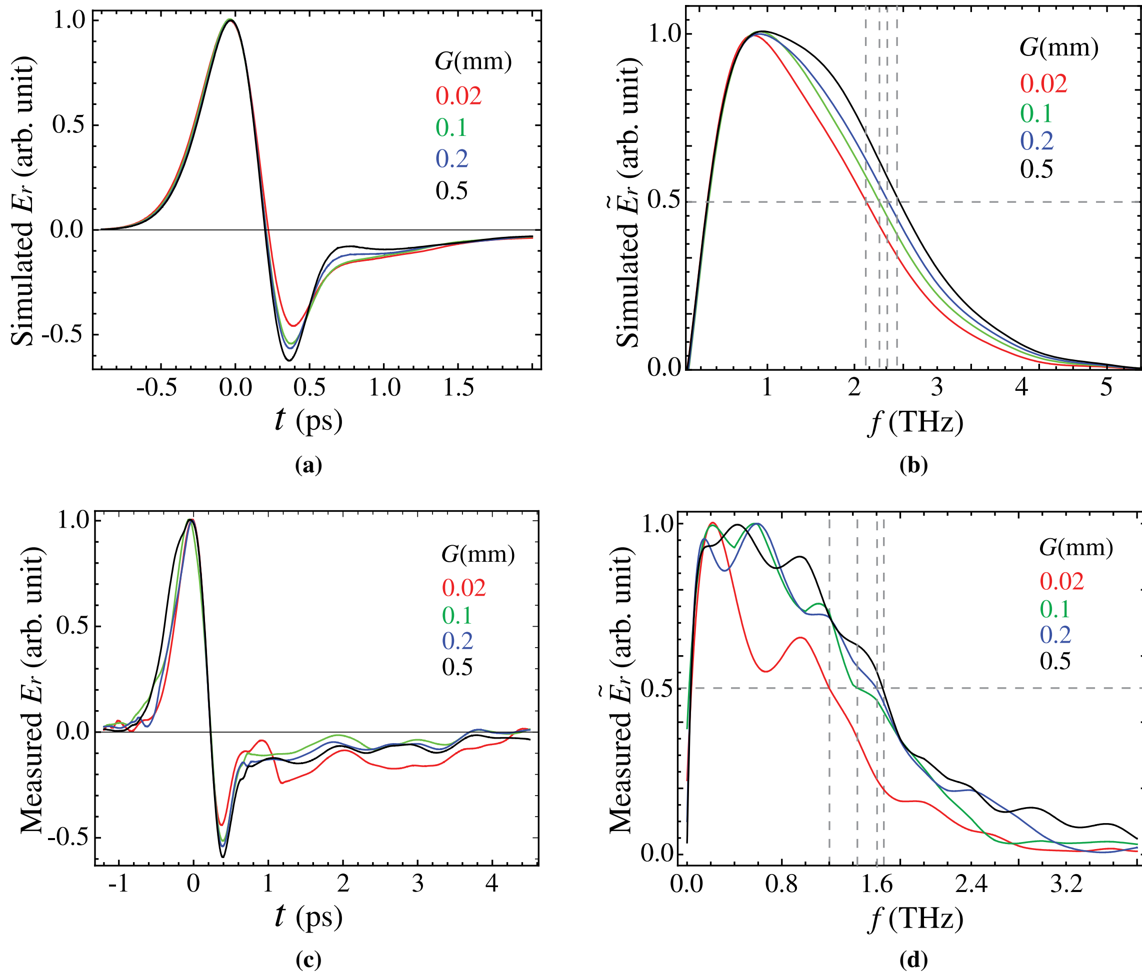


Fig. 6. (Color online) (a) Simulated and (c) measured THz radiation waveforms $E_r$ as a function of time delay $t$ for gap sizes of 0.02 (blue), 0.1 (green), 0.2 (red), and 0.5 mm (black). (b, d) Corresponding Fourier-transformed amplitude $\tilde{E}_r$ spectra. The pump fluence is 70 μJ/cm$^2$.

increases from 0.02 to 0.5 mm, the measured $-E_r^{min}$ increases monotonically from 0.46 to 0.58, and depends in a strongly nonlinear way on $G$. The nonlinear dependence of the measured $-E_r^{min}$ on $G$ can be described using a saturation function with the form $-E_r^{min} = (0.45G^{0.198} + 0.24)/(1 + 0.14G)$, which is also plotted in Fig. 7. The increasing trend in $-E_r^{min}$ reflects the variation of $\Delta f$ and enables $\Delta f$ to exhibit an increasing trend similar to $r$. In detail, the measured $\Delta f$ increases nonlinearly from 1.2 to 1.6 THz with increasing $G$. These $\Delta f$ values are close to those reported by Katzenellenbogen and Grischkowsky[26] ($\Delta f \sim 1.32$ THz) and Tani *et al.*[14] ($\Delta f \sim 1.63$ THz). What is particularly interesting is that such large $\Delta f$ is much larger than those obtained from some large-aperture SI-GaAs antennas ($\Delta f \sim 0.27$ THz),[5] as well as some small-aperture SI-GaAs or multi-GaAs:As$^+$ antennas ($\Delta f \sim 1$ THz).[12] This larger $\Delta f$ is a reflection of a narrow negative peak in Figs. 5(c) and 5(d), and it is just favorable for applications such as THz medical or security imaging requiring broader spectra.

Compared with the measured data in Fig. 7, one can perceive that either the simulated $-E_r^{min}$ or $\Delta f$ vary with $G$ in a manner similar to the measured ones. Fits to the simulated $-E_r^{min}$ yield a saturation function using the form $-E_r^{min} = (4.42G + 0.43)/(1 + 6.66G)$ as plotted in Fig. 7.

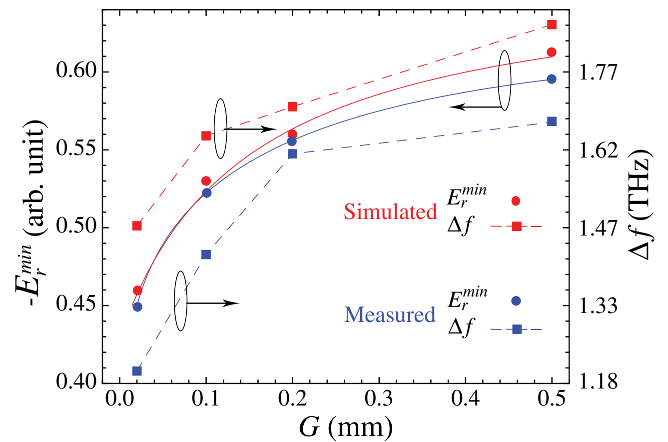


Fig. 7. (Color online) The negative values $-E_r^{min}$ (circles) of the negative peak of THz waveform, and frequency bandwidth $\Delta f$ (squares and dashed curves) versus gap size $G$ for simulation (blue) and measurement (red). The blue and red solid curves are the fits to the simulated and measured $-E_r^{min}$. To compare with the measured $\Delta f$, the values of the simulated $\Delta f$ have been shifted downward by 0.5 THz.

The values of the simulated $-E_r^{min}$ agree well with the measured results, while the simulated $\Delta f$ was found to be larger than the measured ones. This inconsistency is because

our simulation neglects some pulse broadening factors such as the THz pulse dispersion in optical elements, and the strong diffraction property of the THz beam optics. In addition, we also ignore the antenna effect in the 100-μm-wide transmission lines where the field traveling in the $x$-direction is reflected and transmitted into free space (or into the substrate) at the edge of the line owing to the large impedance mismatch between the metal and the semiconductor. This antenna effect might be one of the reasons why the experimental pulse width of THz radiation is broader than that of the theoretical one. However, it is reasonable to guess that the overall characteristics of the THz radiation is determined by the THz field generated in the photoconductive gap, and the antenna effect only broadens the pulse shape without changing the qualitative characteristics of the THz radiation. We consider that this antenna effect is worth investigating further in a future project.

The results of Figs. 5, 6, and 7 imply that the underlying mechanism giving rise to the increasing trend in $-E_{\rm r}^{\rm min}$ is that $-E_{\rm r}^{\rm min} \propto -\partial E_{\rm s}/\partial t$. In other words, $-E_{\rm r}^{\rm min}$ is proportional to the space-charge screening effect. Therefore, an antenna with a larger $G$ will create a stronger space-charge field screening effect leading to larger $-E_{\rm r}^{\rm min}$ and $\Delta f$.

## 5. Conclusions

We have presented a combined experimental and theoretical study of gap-size-dependent effects on THz radiation. Experimentally, we used four multi-GaAs:As$^{+}$ mid-size-gap antennas with different bias voltages and gap sizes to observe their bipolar THz waveforms in the optical pump–probe experiment. At fixed fluence excitation, an increasing trend was observed from either the negative value of the negative peak of terahertz waveform or the bandwidth as the antenna's gap increases. The bandwidths of the THz radiations from our antennas are considerably larger than those from other small-gap or large-aperture antennas. From the waveform shape, it was also found that the width of the positive peak is larger than that of the negative one.

Theoretically, we adopted a rigorous model incorporating trap-enhanced bias fields with a set of electromagnetic wave and drift-Poisson equations to interpret our experimental discovery. The numerical simulations demonstrate the carrier and field dynamics under pump pulse propagation within antennas, and also reproduce the THz waveforms that account for the experimental observations, including increasing trends in both the negative value of the negative peak of THz waveform and the bandwidth, larger peak widths, as well as long waveform tails. Our numerical study indicates that an antenna with larger $G$ has a higher trap-enhanced bias field near the edge of the anode, resulting in a larger space-charge screening effect and bandwidth.

The results will help us understand the mechanisms responsible for gap-dependent THz radiations, and also enable the researchers to realize how to obtain what they need by controlling suitable experimental conditions.

**Acknowledgments**

This work was partially supported by the Academic Top Universities Program of the Ministry of Education and various grants from the National Science Council, Republic of China. Dr. Tze An Liu is gratefully acknowledged for the discussion on THz experiment.

1) D. Grischkowsky, S. Keiding, M. van Exter, and Ch. Fattinger: J. Opt. Soc. Am. B **7** (1990) 2006.
2) R. A. Cheville and D. Grischkowsky: Appl. Phys. Lett. **67** (1995) 1960.
3) R. W. McGowan, R. A. Cheville, and D. Grischkowsky: Appl. Phys. Lett. **76** (2000) 670.
4) B. B. Hu and M. C. Nuss: Opt. Lett. **20** (1995) 1716.
5) T. Hattori, K. Tukamoto, and H. Nakatsuka: Jpn. J. Appl. Phys. **40** (2001) 4907.
6) C. Fattinger and D. Grischkowsky: Appl. Phys. Lett. **53** (1988) 1480.
7) P. U. Jepsen and S. R. Keiding: Opt. Lett. **20** (1995) 807.
8) P. U. Jepsen, R. H. Jacobsen, and S. R. Keiding: J. Opt. Soc. Am. B **13** (1996) 2424.
9) M. S. Markram-Ebied: in *Semi-Insulating III–V Materials*, ed. D. Look (Shiva Publishing, Orpington, U.K., 1984).
10) S. E. Ralph and D. Grischkowsky: Appl. Phys. Lett. **59** (1991) 1972.
11) C. Baker, C. E. Norman, J. A. Cluff, W. R. Tribe, B. E. Cole, E. H. Linfield, A. G. Davies, D. D. Arnone, and M. Pepper: IEEE 10th Int. Conf. Terahertz Electronics Proc., 2002, p. 121.
12) T. A. Liu, M. Tani, and C. L. Pan: J. Appl. Phys. **93** (2003) 2996.
13) J. Lloyd-Hughes, E. Castro-Camus, M. D. Fraser, C. Jagadish, and M. B. Johnston: Phys. Rev. B **70** (2004) 235330.
14) M. Tani, S. Matsuura, K. Sakai, and S. Nakashima: Appl. Opt. **36** (1997) 7853.
15) E. Sano and T. Shibata: IEEE J. Quantum Electron. **26** (1990) 372.
16) G. Rodriguez and A. J. Taylor: Opt. Lett. **21** (1996) 1046.
17) D. S. Kim and D. S. Citrin: J. Appl. Phys. **101** (2007) 053105.
18) S. Hughes, M. Tani, and K. Sakai: J. Appl. Phys. **93** (2003) 4880.
19) M. Sirbu, S. B. P. Lepaul, and F. Aniel: IEEE Trans. Microwave Theory Tech. **53** (2005) 2991.
20) C. M. Hurd and W. R. McKinnon: J. Appl. Phys. **75** (1994) 596.
21) W.-C. Chen and C.-S. Chang: J. Appl. Phys. **81** (1997) 7295.
22) E. J. Rothwell and M. J. Cloud: *Electromagnetics* (CRC Press, New York, 2001).
23) J. W. Goodman: *Introduction to Fourier Optics* (McGraw-Hill, New York, 1996).
24) M. B. Ketchen, D. Grischkowsky, T. C. Chen, C.-C. Chi, I. N. Duling III, N. J. Hala, J.-M. Halbout, J. A. Kash, and G. P. Li: Appl. Phys. Lett. **48** (1986) 751.
25) Q. Wu and X.-C. Zhang: Appl. Phys. Lett. **67** (1995) 3523.
26) N. Katzenellenbogen and D. Grischkowsky: Appl. Phys. Lett. **58** (1991) 222.